Journal of
Materials Chemistry A

ROYAL SOCIETY
OF CHEMISTRY

PAPER

View Article Online
View Journal | View Issue

Check for updates

Cite this: *J. Mater. Chem. A*, 2024, **12**, 24428

Enhanced thermal conductivity and reduced thermal resistance in carbon fiber-based thermal interface materials with vertically aligned structure†

Zhenbang Zhang,[ab] Rongjie Yang,[a] Yandong Wang,[a] Kang Xu,[a] Wen Dai,[a] Jianxiang Zhang,[a] Maohua Li,[a] Linhong Li,[a] Yingying Guo,[a] Yue Qin,[a] Boda Zhu,[a] Yiwei Zhou,[a] Xingye Wang,[a] Tao Cai,[ac] Cheng-Te Lin,[ac] Kazuhito Nishimura,[ac] Hao Nan Li,*[b] Nan Jiang*[ac] and Jinhong Yu*[ac]

Received 6th June 2024
Accepted 2nd August 2024

DOI: 10.1039/d4ta03924f

rsc.li/materials-a

As electronic devices advance, there's a critical need for thermal interface materials (TIMs) with high thermal conductivity and minimal resistance to address thermal dissipation challenges effectively. Carbon fibers (CFs), known for their axial thermal conductivity, are ideal for creating high-performance TIMs in a vertically aligned structure, aligning with the TIMs' heat transfer direction. Despite advancements in CF alignment for improved thermal conductivity, the high thermal resistance and the need for cost-effective manufacturing remain challenges. We propose a novel sandwich structure integrating vertical heat transfer pathways with surface modification to tackle these issues. This structure features a core of vertically aligned CF composite, achieved through a rolling-press method, flanked by liquid metal-modified layers to reduce contact thermal resistance. Our composites demonstrate an exceptional through-plane thermal conductivity of 51.90 W m^{-1} K^{-1} at 73.68 wt% filler content, 323 times higher than that of the PDMS matrix, and a reduced total thermal resistance from 0.55 to 0.32 K cm^2 W^{-1} after interface modification. This research offers insights into designing CF-based composites for enhanced thermal management, applicable in cloud computing and autonomous driving.

Introduction

In recent years, there has been rapid advancement in semiconductor technology, driving silicon-based chips towards more precise manufacturing processes and innovative three-dimensional chip stacking techniques, while introducing new third-generation semiconductor materials like gallium nitride (GaN) and silicon carbide (SiC), applied extensively in 5G base stations, ultra-fast charging stations, and consumer electronics.[1–3] The advancements in processes and novel materials have led to enhanced chip performance but have also resulted in significant heat accumulation issues. Insufficient dissipation of heat could compromise the reliability and stability of electronic devices during their operation, potentially threatening their longevity.[4] To control the operational temperature of chips, ensuring efficient heat transfer from the chips to the heat sink is a crucial step in addressing this challenge. Thermal interface materials (TIMs) have been developed to bridge the mating interface between chips and heat sinks, eliminating air gaps and enhancing effective heat transfer between them.[5,6] The ideal TIMs not only possess high through-plane thermal conductivity ($\kappa_\perp$) but also exhibit low contact thermal resistance (R_{contact}) with the heater and heat sink.[7] In general, TIMs with low R_{contact} require compressibility and flexibility to ensure a greater effective contact area between the mating surface under normal packaging conditions. Due to their flexibility, unique design freedom, and cost-effectiveness, polymers have become the predominant matrix in the most common TIMs. However, the low thermal conductivity of polymers, due to their amorphous arrangement and molecular chain vibrations, restricts their direct application in thermal management.[8] The most effective strategy to enhance thermal conductivity is by introducing micro and nanoscale fillers with high intrinsic thermal conductivity into polymer composites.[9,10] The currently used thermally conductive fillers are generally classified into three categories: ceramics (Al_2O_3,[11] SiC,[12] AlN,[13]

---

[a] *Key Laboratory of Marine Materials and Related Technologies, Zhejiang Key Laboratory of Marine Materials and Protective Technologies, Ningbo Institute of Materials Technology and Engineering, Chinese Academy of Sciences, Ningbo 315201, China. E-mail: yujinhong@nimte.ac.cn*

[b] *Nottingham Ningbo China Beacons of Excellence Research and Innovation Institute, University of Nottingham, Ningbo, China*

[c] *Center of Materials Science and Optoelectronics Engineering, University of Chinese Academy of Sciences, Beijing 100049, China*

† Electronic supplementary information (ESI) available. See DOI: https://doi.org/10.1039/d4ta03924f

BN[14]), metals (Cu,[15] Ag,[16] Al,[17] Ga,[18] In[19]), and carbon materials (diamond,[20] graphite,[21] graphene,[22] CFs,[23] CNT[24]).

Thermal conductivity enhancement relies not only on filler loading but also on the morphology of the fillers (including size, aspect ratio, and alignment) and the interfacial thermal resistance between fillers and the substrate.[9] Previous research findings indicate that fillers with high aspect ratios surpassing the percolation threshold establish continuous heat transfer pathways, achieving efficient heat transfer. Pitch-based carbon fibers (CFs), as one of the prime candidates for high thermal conductivity fillers, exhibit ultra-high axial thermal conductivity (900 W m^{-1} K^{-1}) and outstanding thermal stability.[25] Their high aspect ratios and micron lengths facilitate easier alignment and interconnection, forming continuous thermal pathways to augment the thermal conductivity of composites. To maximize the thermal transport capabilities of CFs, numerous strategies have been reported to achieve their vertical alignment within polymer matrices. These strategies include ice-templating,[26] electrostatic flocking,[27] magnetic field assistance,[28] stress-induced orientation,[29] and flow-assisted methods.[30] Ma *et al.* utilized a vertical freeze-drying method to fabricate a 3D CF skeleton, resulting in an epoxy composite with a through-plane thermal conductivity of 2.84 W m^{-1} K^{-1} at only 13 vol% filler content.[31] Wu *et al.* applied gravity-driven ice-template methods to establish a horizontal CF heat transfer pathway, achieving an in-plane thermal conductivity of 7.98 W m^{-1} K^{-1} at a 22.3 vol% CF content in the composite.[32] Due to limitations in the ice crystal growth-driving force, achieving consistent orientation at high filler content becomes challenging. Huang *et al.* prepared PDMS composites employing a flow-field technique to bridge Al_2O_3 particles with vertically aligned CFs, achieving a through-plane thermal conductivity of 38.0 W m^{-1} K^{-1} with 24 vol% CFs and 47 vol% Al_2O_3.[33] In Han's work, they controlled the orientation of diamagnetic CFs by manipulating the direction of the magnetic field, achieving a maximum thermal conductivity of 45.01 W m^{-1} K^{-1} in the composite.[34] Despite researchers employing various techniques to orient CFs and achieving outstandingly high thermal conductivity, the actual heat transfer efficiency of these as TIMs remains unsatisfactory. The mating surfaces of TIMs with vertical CF structures exhibit significantly high R_{contact} when connected to the heat sink and heat source. This is primarily attributed to the raised and uneven height of the CFs on the surface of TIMs. Due to the high modulus of the CFs, they are unable to deform adequately under normal packaging conditions to establish extensive and efficient contact with the heat sink and heat source. The insufficient contact significantly undermines the effectiveness of heat transfer across the mating interface, presenting a common challenge encountered by nearly all vertically aligned CF-TIMs. To achieving genuinely efficient heat transfer requires not only advancing the $\kappa_\perp$ of vertically aligned CF-TIMs through structured modulation but also optimizing the contact status between TIMs and the heater/heat sink to minimize the R_{contact}.

Herein, we developed a sandwiched structure incorporating a dual strategy of vertical heat conduction pathways and interface modification. The middle layer features vertically aligned CF heat conduction pathways to enhance $\kappa_\perp$, while the upper and lower layers consist of liquid metal-modified layers to reduce R_{contact}. The rolling–stacking process employed in this study enables the continuous and large-scale fabrication of composites featuring a vertically oriented CF structure. Based on its rational structural design, the vertically aligned CF and BN (VCB) composite achieved a maximum $\kappa_\perp$ of 51.90 W m^{-1} K^{-1}, while also exhibiting outstanding thermal stability and good compressibility. Additionally, the introduced liquid metal-modified coating transformed the contact state at the interface from "elastomer–solid" to "liquid–solid" due to which the total thermal resistance of TIMs decreased to 0.32 K cm^2 W^{-1}. Moreover, the impact of the vertically aligned CF structure on the thermal conductivity of the VCB composite under compressive deformation was discussed. In real dynamic applications like CPU cooling down, the VCB composite demonstrated outstanding heat transfer capabilities. This work provides new insights into the design and fabrication of CF-based composites, leveraging their vertical structure and superior heat dissipation performance, offering potential solutions for high-power, high-frequency chips, and consumer electronics in thermal management.

Experimental section

Materials

The mesophase pitch carbon fiber (XN100, NGF) was procured from Fujian United New Material Technology Co., Ltd in Fujian, China. Hexagonal boron nitride (h-BN) was sourced from Momentive Co., Ltd. Polydimethylsiloxane (PDMS) was obtained from Shenzhen HFC Co., Ltd. The liquid metal (GaInSn alloy) was procured from Hunan Sinen Materials Co., Ltd. Additionally, the CF thermal pad (WT5902, $\kappa = 25$ W m^{-1} K^{-1}) was purchased from Tianjin WaermTimo New Material Technology Corp., Ltd in Tianjin, China.

Preparation of VCB composites

The first step involves preparing a homogeneous mixture solution of PDMS and fillers, where the uniformity and rheological properties of the mixture solution significantly impact the subsequent CF orientation process. Initially, the two components of PDMS, A and B, are mixed in a 1 : 1 ratio using a high-speed mixer (2000 rpm, 2 minutes) to achieve uniformity. Subsequently, a predetermined proportion (55, 60, 65, 70, and 73.68 wt%) of CFs and BN fillers (maintaining a fixed ratio of 8 : 1 for CFs to BN) is added to the prepared PDMS solution. Due to the high filler content, achieving uniform mixing of the solution requires multiple sequential additions of fillers during the mixing process. This step also involves the use of a high-speed mixer operating at 2000 rpm for a duration of 5 minutes to ensure thorough mixing. The second step involves orienting the CFs using a roll press machine. The uncured mixed solution is poured into the hopper of the roll press machine, with a layer of PET film placed above and below (to maintain the shape of the uncured material). The distance between the dual rollers is adjusted to control the degree of fiber orientation, with the rollers operating at a controlled speed of 60 cm min^{-1}.

Subsequently, the oriented thin-layered CF composite is cured for 12 hours at 80 °C. The third step involves preparing block-shaped composites. Post-curing, the high-viscosity thin-layered composite necessitates the removal of PET film with the assistance of liquid nitrogen. A stacking-friendly shape is achieved by using a template cutter along the fiber orientation direction. Finally, the stacked composite is placed in a specialized mold and subjected to a pressure of 20 MPa to densify the composites. Subsequently, the block-shaped composite material is sliced along a specific direction using an ultrasonic cutter.

Preparation of VCB-LM composites

Initially, the prepared VCB composite was positioned on the sample stage of the vacuum thermal evaporation equipment. Subsequently, an appropriate amount of GaInSn liquid metal was poured into the tungsten evaporator boat. The sample chamber was then sealed, and the chamber was evacuated until reaching a vacuum level of 3×10^{-3} Pa. Following this, a heating current of 300 A was applied to the tungsten crucible to initiate the deposition of the liquid metal. The deposition process lasted for 2 minutes until reaching a deposition thickness of 10–15 μm. Subsequently, using the same procedure, the liquid metal was deposited on the backside of the sample.

Characterization

The microstructures and morphological characteristics of the CFs, boron nitride, and VCB composites were examined using a scanning electron microscope (SEM, HITACHI, SEM Regulus 8230, Japan). The crystallographic properties of the CFs and boron nitride were analyzed *via* X-ray diffraction (XRD, Bruker, D8 Discover, Germany, utilizing Cu Kα radiation). Raman spectroscopy was conducted using a Raman spectrometer (HORIBA, LabRAM Odyssey, France) with a 532 nm wavelength laser. The three-dimensional (3D) structure of the VCB composites was reconstructed using X-ray computed tomography (micro-CT) images processed *via* Dragonfly software. Micro-CT images were acquired using an X-ray three-dimensional imaging system (micro-CT, ZEISS Xradia 610 Versa, Germany). X-ray diffraction patterns were obtained utilizing a Wide-Angle X-ray Diffraction (WAXD, Xeuss 2.0, Xenocs, France) system, employing a copper source with an X-ray beam wavelength of 1.54 Å and a power of 30 W. The thermal conductivity (κ) of the composites was determined using the formula: $\kappa = \alpha \times \rho \times C_\mathrm{p}$, where α, ρ, and C_p represent the thermal diffusivity, density, and specific heat, respectively. The thermal diffusivity of the composites was measured using a laser flash apparatus (NETZSCH, LFA 467, Germany). Specific heat was determined through differential scanning calorimetry (NETZSCH, DSC 214, Germany). The thermal resistance was measured using a thermal resistance tester (Longwin, LW9389) in accordance with the ASTM D 5470-06 standard. Density was assessed *via* the average density obtained using the water displacement method. The compression stress and strain of VCB composites were tested using a universal testing machine (UTM, Roell Z030, Zwick, Germany). An infrared camera (Fluke, Ti400, USA) was employed to record temperature evolution.

Results and discussion

Preparation and structural characterization of the VCB composites

The preparation process of composites involves techniques such as rolling press orientation, stacking, cold pressing, and directional slicing, as depicted in the comprehensive fabrication flowchart in Fig. 1a. The industrial acceptance of rolling press technology stems from its capability to produce continuous products in large quantities. Within this process, rolling press stands out as a crucial step for aligning CFs. Under the torque induced by shearing flow, short fibers gradually rotate and align along the spreading direction, resulting in the anisotropy observed in the final products.[35] The SEM image in Fig. 1b exhibits a single-layer composite extruded using a rolling machine, showcasing a structured alignment. The spacing between the dual rolls is a critical factor in determining the degree of fiber orientation. We fabricated a series of single-layer samples with varying spacings, and the orientation structures of these samples are depicted in Fig. S1.† When the spacing between the rolls was less than or equal to 400 μm, a highly oriented arrangement was consistently achieved. However, as the spacing increased to 500 μm, the orientation began to become more chaotic, and at 700 μm, the orientation significantly deteriorated. Therefore, we have chosen to use a 400 μm roller spacing for sample fabrication, balancing good orientation structure with improved production efficiency. Furthermore, samples of VCB-73.68 wt%-*X* were prepared according to the same fabrication process with varying roller pressing thicknesses (250–700 μm). The results (Fig. S2†) demonstrate that VCB-73.68 wt%-*X* samples prepared with a roller pressing thickness of 400 μm exhibit the highest thermal conductivity. Examination confirms the widespread directional arrangement of CFs, validating the effectiveness of the rolling orientation technique. The production of large bulk composites with an oriented structure involves the directional stacking of composites rolled in single layers. The unique cross-linked structure of PDMS results in a certain level of adhesion on the cured sample surface, allowing the layers of stacked material to compact solely through cold pressing.[36] To test the adhesive properties of the single-layer composite, we attached one end of the composite to a steel plate and the other end to another strip of composite, as shown in Fig. S3.† When suspended, no cracks were observed at the bonding site. Subsequently, ultrasonic cutting was employed to obtain vertically structured CF composites from the block-shaped composites. Fig. 1c illustrates the surface of the prepared composites, indicating that the CFs are not covered by the matrix. Additionally, the cross-sectional image in Fig. 1d exhibits a highly vertical CF structure within the composites. Consequently, these structural features endow the composites with exceptional through-plane thermal transfer properties. Fig. S4† presents optical images detailing each procedural step, while Fig. S5† showcases optical images of the batch-produced products post-slicing. Fig. S6†

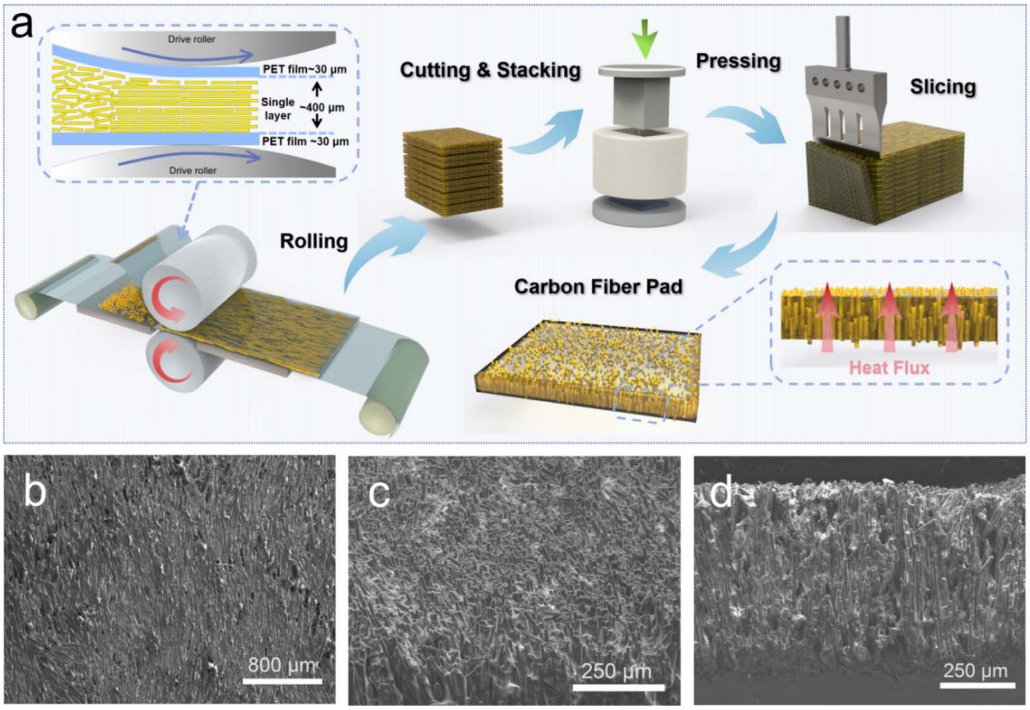

Fig. 1 Preparation and morphology of the VCB TIMs. (a) Schematic diagram of the rolling-press technique for aligning carbon fibers and the production process of VCB composites. (b) The microstructure of continuous single layer composites extruded by the roller. (c and d) Top view and cross-section view of the microstructure of VCB composites.

shows the VCB composite under bending conditions. Even at large bending angles, no delamination or cracking was observed between the layers.

The strategy of this study involves filling polymers with fillers and modifying their arrangement to enhance the thermal conductivity of composites. Consequently, the properties and dimensions of the fillers will directly impact the overall performance of the composites. In our study, high thermal conductivity short chopped pitch-based CFs were chosen as the primary filler to enhance the thermal conductive of the composite. Fig. S7a–c† depict the optical, SEM magnified, and microstructural images of CFs. According to the images, the diameter of the CFs measures 10 μm, with a length of 250 μm (as detailed in the length distribution in Fig. S7d†). Furthermore, the fiber cross-section displays the characteristic radial folded arrangement indicative of mesophase pitch-based CFs. The XRD pattern of the CFs displayed in Fig. S7e† exhibits characteristic peaks associated with graphite, and the peak at 26.4° corresponds to the (002) plane, while the prominent peak at 54.5° is assigned to the (004) plane. These sharp characteristic peaks indicate larger grain sizes, smaller interlayer spacing, and a closely packed arrangement of graphite layers, consistent with the cross-sectional image in Fig. S7c.†[37] The Raman spectrum of the CFs is depicted in Fig. S7f,† wherein distinct peaks at 1353, 1582, and 2704 cm^{-1} labeled as D, G, and 2D, respectively, were observed. These peaks are commonly employed to characterize the structure of carbon materials, and the I_D/I_G ratio of the CFs serves as a pivotal metric for assessing their thermal conductivity. The I_D/I_G value of the CFs utilized in this study is 0.135, indicating remarkably low defects and superior thermal conductivity. h-BN serves as the second hybrid filler in this study. Its role includes filling the gaps between CFs, bridging these fibers to establish additional thermal pathways. Furthermore, it aids in modulating the rheological properties of the uncured mixed solution. The optical and SEM magnified images of the h-BN are presented in Fig. S8a–c.† The h-BN exhibits a lateral size range of 20–50 μm, as depicted in the lateral size distribution plot in Fig. S8d,† with a thickness of 1–2 μm. Fig. S8e† displays the XRD pattern of BN, showcasing distinct characteristic peaks. Additionally, Fig. S8f† presents the prominent Raman peak at 1365 cm^{-1} for h-BN. These results confirm the excellent crystal quality of the larger-sized BN.

Based on their fabrication method, the produced block-shaped composites exhibit anisotropic characteristics. To explore their internal structure and the influence of fiber orientation on performance, samples were sliced along the direction indicated in the schematic diagram in Fig. 2a. The composites cut along the direction perpendicular to the Cartesian coordinate system's *X*-axis are denoted as VCB-*X*, featuring a vertical CF alignment within their interior. Correspondingly, samples cut along the direction perpendicular to the *Y* and *Z* axes are denoted as VCB-*Y* and VCB-*Z*, respectively. To analyze the internal structure, we used an advanced micro-CT tool to scan the VCB-*X*, VCB-*Y* and VCB-*Z* composites. Within this research, the angle between the fibers and the *Z*-axis (through-plane direction) was defined as θ, as illustrated in Fig. 2b. Furthermore, the CF skeleton inside the three composites is shown in Fig. 2c (where fibers at different angles are

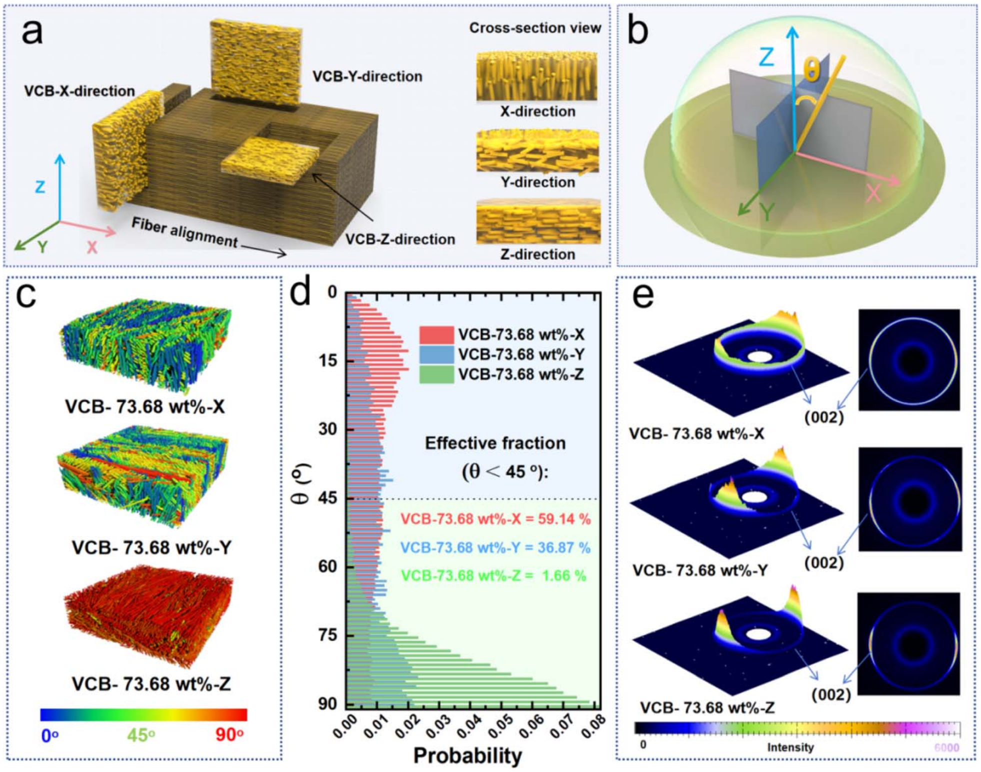

Fig. 2 Microstructure characterization of VCB composites. (a) Schematic diagram of the anisotropic composite cutting method (VCB-*X*, VCB-*Y* and VCB-*Z* are prepared by cutting vertically along the *X*, *Y* and *Z* axes, respectively). (b) Schematic of the angle (θ) between CFs and the normal vector in the 3D model. (c) Micro-CT model of VCB 73.68 wt%-*X*, VCB 73.68 wt%-*Y* and VCB 73.68 wt%-*Z* composites. (d) Probability statistical plot of CF angle distribution according to the micro-CT model. (e) 3D and 2D WAXD patterns for VCB composites.

represented by distinct colors). ESI Video S1† showcases the angular distribution of CFs in the three specimens. Subsequently, reconstruction of models was conducted using analysis software, generating the fiber angle distribution data within each composite, as depicted in Fig. 2d. By comparing the data from the three specimens, the angular distribution of the VCB-73.68 wt%-*X* specimen follows a normal distribution centered at 15°. Correspondingly, the model predominantly exhibits blue and green colour, which aligns with our deliberately controlled outcome (smaller angular distributions indicate higher alignment degrees). However, in VCB-73.68 wt%-*Y*, the distribution appears more random, leading to a relatively chaotic pattern in the model. However, the VCB-73.68 wt%-*Z* sample exhibits a predominance of larger angular distributions, resulting in a higher uniformity in the model colors. Yet, due to the low radial thermal conductivity of CFs, this orientation in this direction does not favor through-plane heat conduction. Considering the significantly higher axial thermal conductivity of the anisotropic CFs compared to their radial counterpart, we introduced the parameter of "effective fraction". When θ is less than 45°, it signifies a higher contribution to heat conduction; however, angles greater than 45° contribute less. Through calculations, the VCB-73.68 wt%-*X* sample exhibited an effective fraction of 59.14%, VCB-73.68 wt%-*Y* measured 36.87%, while VCB-73.68 wt%-*Z* was only 1.66%. Wide-angle X-ray diffraction (WAXD) was utilized to assess the degree of orientation in composites. CFs comprise stacked layers of hexagonal carbon networks preferentially oriented along the fiber axis, with the structural and orientational characteristics revealed by the XRD peak originating from the (002) crystal plane reflection of these carbon network layers.[38,39] Employing this technique, an analysis was conducted on three variants of VCB composites, and the resultant 3D and 2D patterns are visually presented in Fig. 2e. During the test, X-rays directly pass through the actual heat transfer path of each sample. Due to the vertical distribution of CFs in the VCB-*X* sample, X-rays passing through the axial direction of the fibers do not exhibit noticeable characteristic peaks. However, in the VCB-*Y* and VCB-*Z* samples, X-rays passing through the radial direction of the fibers exhibit distinct peaks that are clustered together. The diffraction peaks of VCB-*Z* have a relatively narrow half-width, consistent with the micro-CT test data. Fig. S9† also displays the integral intensity of the (002) crystal *vs.* azimuth angle curves of the three samples. Through the aforementioned testing methodologies, we have successfully fabricated anisotropic composites with highly oriented structures. Among these, VCB-*X* exhibits the most promising vertical alignment of CFs. This vertical structure establishes the most efficient thermal conduction pathway, greatly enhancing the thermal conductivity efficiency of the thermal interface material.

Thermal conductivity of the VCB composites

To investigate the impact of filler content on the thermal conductivity of anisotropic composites, we prepared samples with varying filler contents (ranging from 55 to 73.68 wt%). Fig. 3a illustrates the influence of filler content on the thermal conductivity in the three directions (*X*, *Y*, *Z*) of the anisotropic VCB composites, and the detailed calculation parameters are available in ESI Table S1.† As the filler content increased, the thermal conductivity of samples in all three directions (*X*, *Y*, *Z*) also increased. However, owing to its structural characteristics, composites with the same filler content exhibited significant differences in through-plane thermal conductivity across different directions. VCB-73.68 wt%-*X* attained the highest thermal conductivity, reaching 51.90 W m^{-1} K^{-1}. In contrast, at the same filler content, VCB-73.68 wt%-*Y* registered 17.32 W m^{-1} K^{-1}, while VCB-73.68 wt%-*Z* exhibited only 2.07 W m^{-1} K^{-1}. It's worth noting that these test results align with the "effective fraction" depicted in Fig. 2c, confirming that the angular distribution of CFs is the most crucial parameter affecting the thermal conductivity. Next, the anisotropy ratios of the thermal conductivities in different directions, specifically κ_X

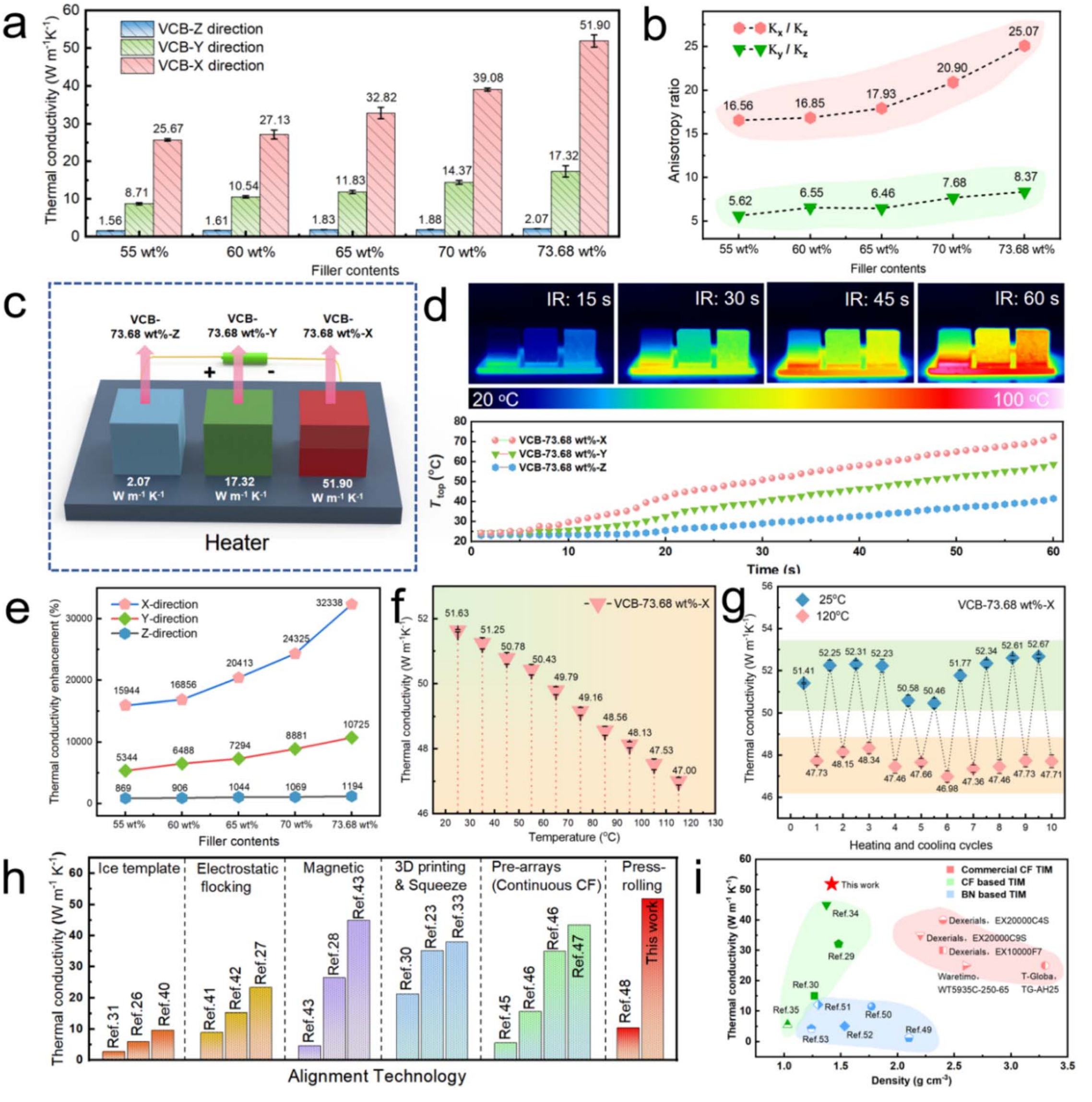

Fig. 3 Thermal properties of VCB composites. (a) Effect of filler contents on thermal conductivities of anisotropic VCB composites in the three directions. (b) Effect of filler contents on anisotropic factor ratio (k_x/k_z and k_y/k_z) of VCB composites. (c) Schematic diagram of the through-plane heat transfer capability test system. (d) Infrared photo and the temperature evolution curves during the heating process for comparing the thermal conductivity of VCB 73.68 wt%-*X*, VCB 73.68 wt%-*Y* and VCB 73.68 wt%-*Z* composites. (e) Effect of filler contents on the thermal conductivity enhancement of anisotropic VCB composites in the three directions. (f) Effect of environmental temperature on the thermal conductivity of the VCB-73.68 wt%-*X* composite. (g) The thermal conductivity variation of VCB-73.68 wt%-*X* during heating and cooling at 10 cycles. (h) The comparison of thermal conductivity among various preparation methods for carbon fiber composites reported in the literature. (i) Comparison of thermal conductivity and density between composites with carbon fiber-based, BN-based, and commercial TIMs as reported in the literature.

to κ_Z and κ_Y to κ_Z, were calculated. The results are illustrated in Fig. 3b. A larger numerical value of the anisotropy ratio indicates a greater difference in thermal conductivity. At the highest filler content, κ_X/κ_Z and κ_Y/κ_Z reached 25.07 and 8.37, respectively. To further validate the varying heat transfer capabilities in different directions of the anisotropic composites, we set up a system, as depicted in Fig. 3c, employing an infrared camera to record the temperature rise rates of VCB-73.68 wt%-*X*, VCB-73.68 wt%-*Y*, and VCB-73.68 wt%-*Z*. Fig. 3d displays the infrared images captured at different time intervals and the temperature data curves at the top of the samples under identical test conditions for the three samples. From the IR images, it's evident that VCB-73.68 wt%-*X* exhibits the fastest heat transfer rate, resulting in a more uniform temperature distribution across the material. Conversely, VCB-73.68 wt%-*Z*, due to its lower thermal conductivity, impedes heat transfer towards the top, causing most of the heat to concentrate at the interface with the heat source. The disparities in temperature curves further corroborate the superior through-plane thermal transfer performance of VCB-73.68 wt%-*X*. Moreover, we employed Thermal Conductivity Enhancement (TCE) to express the improvement of the composite's thermal conductivity relative to the pure PDMS matrix. The formula for calculating TCE is as follows:

$$\mathrm{TCE} = \frac{\kappa_\mathrm{c} - \kappa_\mathrm{m}}{\kappa_\mathrm{m}} \times 100\% \tag{1}$$

where κ_c represents the thermal conductivity of the composite, while κ_m stands for the thermal conductivity of the pure matrix. The VCB-73.68 wt%-*X* exhibits an outstanding TCE of 32 338%, as shown in Fig. 3e, whereas the VCB-73.68 wt%-*Z* at the same filler content registers only 1194%. This data further validates the crucial significance of controlling the orientation structure of anisotropic fillers.

Beyond thermal conductivity, thermal stability also dictates the applicability of certain materials. Excellent thermal stability allows materials to perform effectively under extreme operating conditions. Fig. 3f illustrates the thermal conductivity change of VCB-73.68 wt%-*X* across a temperature range of 25 to 115 °C. As expected for many materials, there is a gradual reduction in thermal conductivity with increasing temperature. Fig. 3g records the variations in thermal conductivity during successive heating and cooling cycles, aiming to assess the stability of thermal conductivity under thermal shock conditions. The graph displays ten cycles of heating and cooling. Throughout this phase, VCB-73.68 wt% demonstrates commendable stability, displaying minor fluctuations, both at high and low temperatures. In Fig. 3h, we have compared the thermal conductivity values of previously reported CF-based TIMs with those obtained in this work, considering the preparation techniques employed for oriented CFs. More detailed data can be found in ESI Table S2.† Methods like ice templating[26,31,40] are suitable for fabricating 3D skeletons, yet they fail to provide high thermal conductivity at low filler concentrations. Techniques such as electrostatic flocking[27,41,42] and magnetically assisted methods,[28,34,43] due to their intricate process conditions, have not gained industrial acceptance. Presently, methods involving 3D printing[23,30,33] and flow-assisted extrusion,[44] as well as the pre-arrays[45–47] of continuous CFs, appear to hold promise as potential industrial-scale manufacturing processes for TIMs. It is worth noting that both 3D printing and flow-assisted extrusion techniques seem to have reached a bottleneck in terms of achieving thermal conductivity improvements, as neither has surpassed 40 W m^{-1} K^{-1}. Moreover, while the approach involving continuous pre-alignment of CFs holds promise for achieving higher values, the cost of continuous CFs remains prohibitively high for manufacturers. Therefore, the rolling-press technique[48] employed in this study emerges as a potential method for large-scale production of high thermal conductivity CF-TIMs. The TIMs produced through this method achieved thermal conductivity exceeding 50 W m^{-1} K^{-1}, surpassing all previously mentioned fabrication approaches. The density of TIMs is also a crucial parameter under consideration. In Fig. 3i, a comparison of density *vs.* thermal conductivity is drawn among CF-based TIMs,[29,30,34,45] BN-based TIMs,[49–53] and commercially available CF-based TIMs from previous literature. The detailed parameters are provided in Table S3.† It's observed that most TIMs exhibit a density below 2 g cm^{-3}, owing to the relatively lower density of CFs and boron nitride fillers. However, the thermal conductivity of BN-based TIMs remains below 15 W m^{-1} K^{-1}, unable to meet the requirements for high thermal conductivity. While commercially available CF-TIMs exhibit commendable thermal conductivity, they tend to have higher densities. Contrastingly, the TIMs developed in this study achieve the highest thermal conductivity alongside relatively lower densities. Therefore, this sample demonstrates significant advantages in applications requiring extreme lightweight characteristics, such as aerospace or portable electronic devices.

Furthermore, the rough surface of CF-based TIMs cannot achieve extensive interfacial contact, resulting in an increase in interfacial thermal resistance. Therefore, a low compression modulus allows the TIMs to deform under pressure, enabling them to conform to rough surfaces. Fig. S10† illustrates the compression stress–strain curve of VCB-73.68 wt%-*X*. The curve indicates significant deformation occurring at relatively low pressures, implying that this TIM can achieve excellent conformability even at lower packaging pressures. Another point of interest is that the vertically structured TIMs, upon experiencing deformation under pressure, cause a tilt in the angles of the CFs, as depicted in the schematic diagram of Fig. 4a and S11.† While we aim to prevent tilting, the alteration in the anisotropic structure under substantial deformation is unavoidable. Hence, determining the optimal sealing pressure for anisotropic TIMs is an essential consideration. Fig. 4b illustrates the change in thermal conductivity and thickness of VCB-73.68 wt%-*X* upon deformation under pressures ranging from 10 to 100 psi. It's important to note that the thickness measurements were taken after compression. As depicted in Fig. 4b, with increasing pressure, the thickness of VCB-73.68 wt%-*X* decreased from its original 1.40 to 0.80 mm after compression at 100 psi, concurrently reducing the thermal conductivity from 50.62 to 19.07 W m^{-1} K^{-1}. As evident in Fig. 4c–e, prior to compression, the CFs in the TIMs were

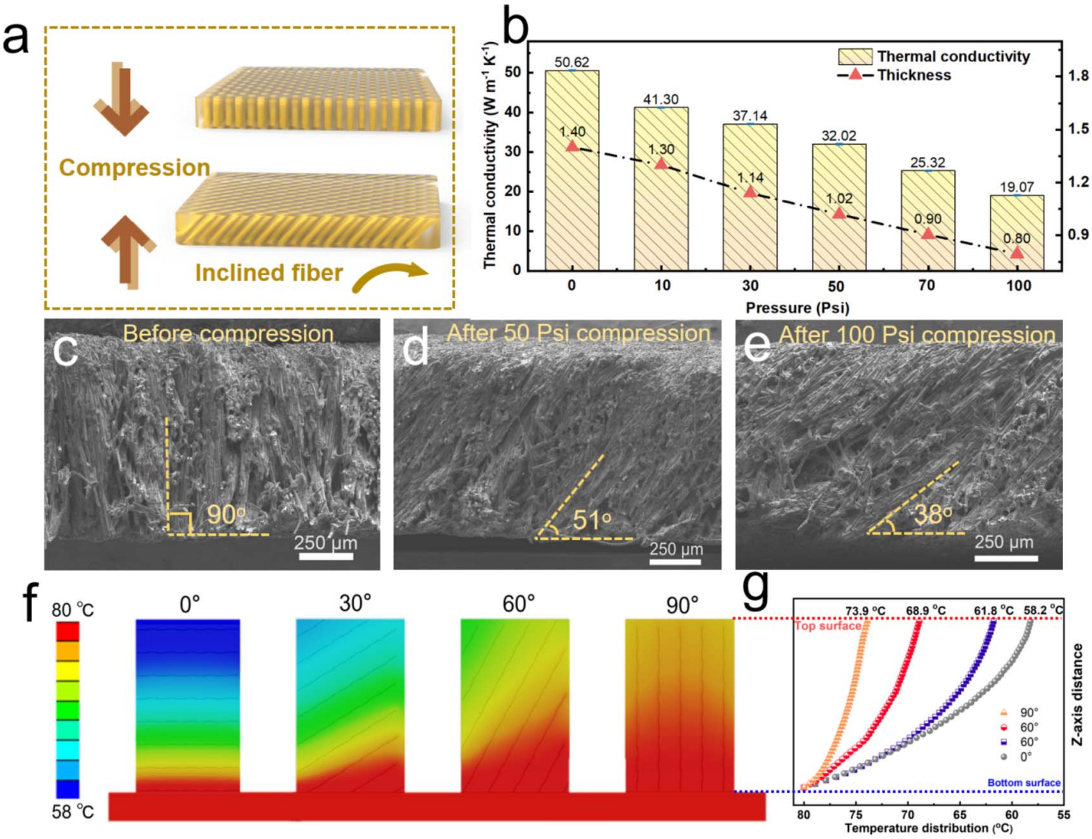

Fig. 4 The influence of pressure on thermal conductivity and structure of the VCB 73.68 wt%-*X* composite. (a) Schematic diagram of deformation of the vertical carbon fiber structure under pressure. (b) Effect of compressive stress on the thermal conductivity of the VCB-73.68 wt%-*X* composite and thickness (samples are measured for thermal conductivity and thickness after pressure release). (c–e) The incline angle of the carbon fiber structure of the sample after different pressure release. (f) Simulation comparison of heat transfer properties of composites with various incline angle CF structures. (g) The temperature gradient distribution curves at the center position calculated by four simulation models.

positioned at a 90° angle to the base. Following compression at 50 psi, the CF angle changed to 51°, further reducing to 38° after compression at 100 psi. Based on the above results, we determined that the optimal packing pressure range for VCB composites is 10–30 psi. Within this range, the inclination angle of the CFs does not change significantly. However, when the pressure exceeds 50 psi, the CFs exhibit excessive inclination, leading to a substantial decrease in thermal conductivity, thus resulting in failure.

To further validate the impact of CF orientation angles on thermal conductivity, finite element analysis was employed for verification. The first step involved establishing four models as depicted in the Fig. S12,† positioned at the same heating plate, while the external surroundings were designated as PDMS substrate with a thermal conductivity of 0.16 W m^{-1} K^{-1}. Within the substrate, CFs were introduced at angles of 0°, 30°, 60°, and 90° respective to the base. The ambient temperature was set at 22 °C, and convective heat transfer conditions were applied to the boundaries of the four models, with a coefficient of 5 W m^{-2} K^{-1}. The heating plate was maintained at a constant 80 °C, ensuring heat conduction from the bottom of the model to the top. The boundary conditions were set for the models, and subsequently, a mesh generation process was applied to the configured models, as depicted in Fig. S13.† Following this, computations were performed, producing temperature distribution maps for the four models, showcased in detail in Fig. 4f. As indicated by the computational outcomes, the inclined angle of CFs significantly influences the temperature distribution within the models. Fig. 4g illustrates the temperature gradient from the bottom to the top within the models. The model with a 0° orientation of CFs exhibits the most significant temperature differential, reaching only 58.2 °C at the top surface. Conversely, the model with a 90° orientation shows the best internal temperature uniformity, reaching 73.9 °C at the top surface. Additionally, the model tilted at 60° demonstrates better temperature uniformity compared to the 30° oriented model. This simulation outcome aligns with our experimental results, indicating that an increase in the tilt angle of CFs leads to a decrease in their thermal conductivity.

Thermal resistance of the VCB composites

Generally, the total thermal resistance is a critical parameter affecting the performance of TIMs during practical applications. When TIMs are used to bond the heater and heat sink, the components of the total thermal resistance (R_{total}) are represented as shown in eqn (2).

$$R_{\text{total}} = R_{\text{bulk}} + R_{\text{contact}} = \frac{\text{BLT}}{k_{\perp}} + \left(R_{\text{heater/TIM}} + R_{\text{heat sink/TIM}}\right) \quad (2)$$

where R_{bulk} stands for the bulk thermal resistance of the TIM, defined as the ratio of bond line thickness (BLT) to the intrinsic $\kappa_{\perp}$; R_{contact} represents the contact thermal resistance, equal to the sum of interface contact thermal resistance of the TIM with the heater ($R_{\text{heater/TIM}}$) and heat sink ($R_{\text{heat sink/TIM}}$). Based on eqn (2), the high through-plane thermal conductivity ($\kappa_{\perp}$) achieved by optimizing the filler orientation structure merely reduces R_{bulk}. R_{contact} stands as another crucial parameter affecting R_{total}. As the original TIMs' surfaces are filled with rigid CFs as shown in Fig. 1c, their imperfect conformity with the heater or heat sink results in a high R_{contact}. To decrease R_{contact} for achieving a lower R_{total}, our approach involved employing a vacuum evaporation technique to coat a liquid metal buffer layer on the upper and lower surfaces of the TIMs, as illustrated in the schematic diagram in Fig. 5a.

In Fig. 5b, the optical images reveal distinct appearances between the original VCB-73.68 wt%-*X* and the liquid metal modified VCB-73.68 wt%-*X*-LM. The original TIM presents a dark, CF-like hue, while the VCB-73.68 wt%-*X*-LM showcases a metallic luster resembling liquid metal. In Fig. 5c, the SEM images display the cross-sectional view of VCB-73.68 wt%-*X*-LM, while Fig. 5d–i illustrate the corresponding elemental distribution maps. These findings provide evidence that the liquid metal has been uniformly applied to the sample surface, with a thickness ranging approximately between 10 and 15 μm. Fig. 5j displays the microscopic morphology of VCB-73.68 wt%-*X*-LM, while Fig. 5k and l illustrate a comparative analysis of the surface structures between VCB-73.68 wt%-*X* and VCB-73.68 wt%-*X*-LM. It's evident that the surface of the original sample is filled with upright CFs and exhibits some pores. The surface roughness (Sa) of the original sample was measured to be 15.29 μm through laser confocal testing, with detailed results illustrated in Fig. S14a–c.† The high surface roughness is a crucial factor affecting R_{contact}. Due to the notably high modulus of CFs and the significantly lower modulus of the PDMS matrix, there is currently no effective method available to achieve a uniformly smooth surface for this composite through mechanical slicing. Surface modification has become an effective way to achieve low roughness for this composite. Through observation, the surface of VCB-73.68 wt%-*X*-LM is entirely covered by the liquid metal, effectively filling the surface pores. The surface roughness (Sa) measures 14.32 μm as shown in Fig. S14d and e.† The limited reduction in surface roughness is attributed to the high surface tension of the liquid metal, causing small droplets to re-aggregate, forming larger droplets. These droplets create surface protrusions, which result in the higher surface roughness. However, this high roughness is deceptive and the protrusions tend to flow, enhancing the conformability of the interface.

As depicted in the schematic diagram in Fig. 5m, under normal packaging pressure, the low-modulus TIMs can undergo some deformation to conform to the rough surfaces of both the heat sink and heater, thereby increasing the effective contact area. However, there still exist tiny voids in micron size that cause thermal resistance. Due to its excellent flowability, liquid metal can almost perfectly fill the voids between interfaces, forming a "solid–liquid–elastomer" structure, significantly increasing the effective contact area and thereby enhancing heat transfer efficiency. Next, we tested the total thermal resistance of VCB-73.68 wt%-*X* and VCB-73.68 wt%-*X*-LM using the ASTM D-5470 standard, and the results are depicted in Fig. 5n. The total thermal resistance of untreated VCB-73.68 wt% ranges from 0.75 to 0.48 K cm^2 W^{-1} under 10–100 psi pressure, decreasing with increasing pressure. However, for VCB-73.68 wt%-*X*-LM samples, the thermal resistance is only 0.44–0.26 K cm^2 W^{-1}. Compared to before modification, there's a significant decrease in total thermal resistance, attributed to the effectiveness of the liquid metal buffer layer. Fig. 5o illustrates a comparison plot presenting the thermal conductivity and total thermal resistances of various types of TIMs reported in previous literature, such as hydrogels,[54,55] thermal pads,[47,56–59] and thermal grease.[60,61] The detailed parameters are outlined in Table S4 of the ESI.† Despite the notably low thermal resistance in certain thermal greases, their thermal conductivity tends to be low, and these low resistances are often measured under extremely thin BLT. In applications demanding thicker BLT, thermal pads demonstrate their advantage. In comparison to other pads, our VCB-73.68 wt%-*X*-LM in this study achieves the highest thermal conductivity and remarkably low thermal resistance. This is evident upon contrast with other existing thermal pads.

Verification of TIM performance and realistic application

To investigate the interfacial heat transfer capacity of the TIMs, we set up the TIM performance test system as illustrated in Fig. 6a. This system utilizes a ceramic heater as the heat source and a temperature-controlled platform as the heat sink. The VCB-73.68 wt%-*X*-LM (size: 10 × 10 × 0.8 mm^3) is placed between these two components, and 50 psi pressure is applied to simulate the real working state of TIMs. It is important to note that Ga alloys exhibit strong corrosiveness towards aluminum and should not come into direct contact with it. It is recommended to use metals with better corrosion resistance, such as nickel or copper, as the direct contact surface with LM, or to use heat sinks with anti-corrosion coatings. The heat generated by the heater passes through the VCB-73.68 wt%-*X*-LM and transfers to the heat sink, and is eventually dissipated by the cooling water. Subsequently, the heat transfer capability of the VCB-73.68 wt%-*X*-LM is verified by monitoring the temperature changes of the heater. For comparison, under the same conditions, the interface heat transfer performance of the unmodified VCB-73.68 wt%-*X* and a commercial CF thermal pad (WT-5902) was also tested. Fig. 6b illustrates the temperature evolution of the heater (T_{heater}) for the three samples under different power densities ranging from 10 to 80 W cm^{-2}. Compared to the commercial TIM, VCB-73.68 wt%-*X* resulted in a decrease of 11.5 °C in heater temperature at a power density of 80 W cm^{-2}, while VCB-73.68 wt%-*X*-LM further reduced it by 54.2 °C. Based on the data in Fig. 6c, the derived equivalent heat transfer coefficients, calculated by taking the reciprocal of the

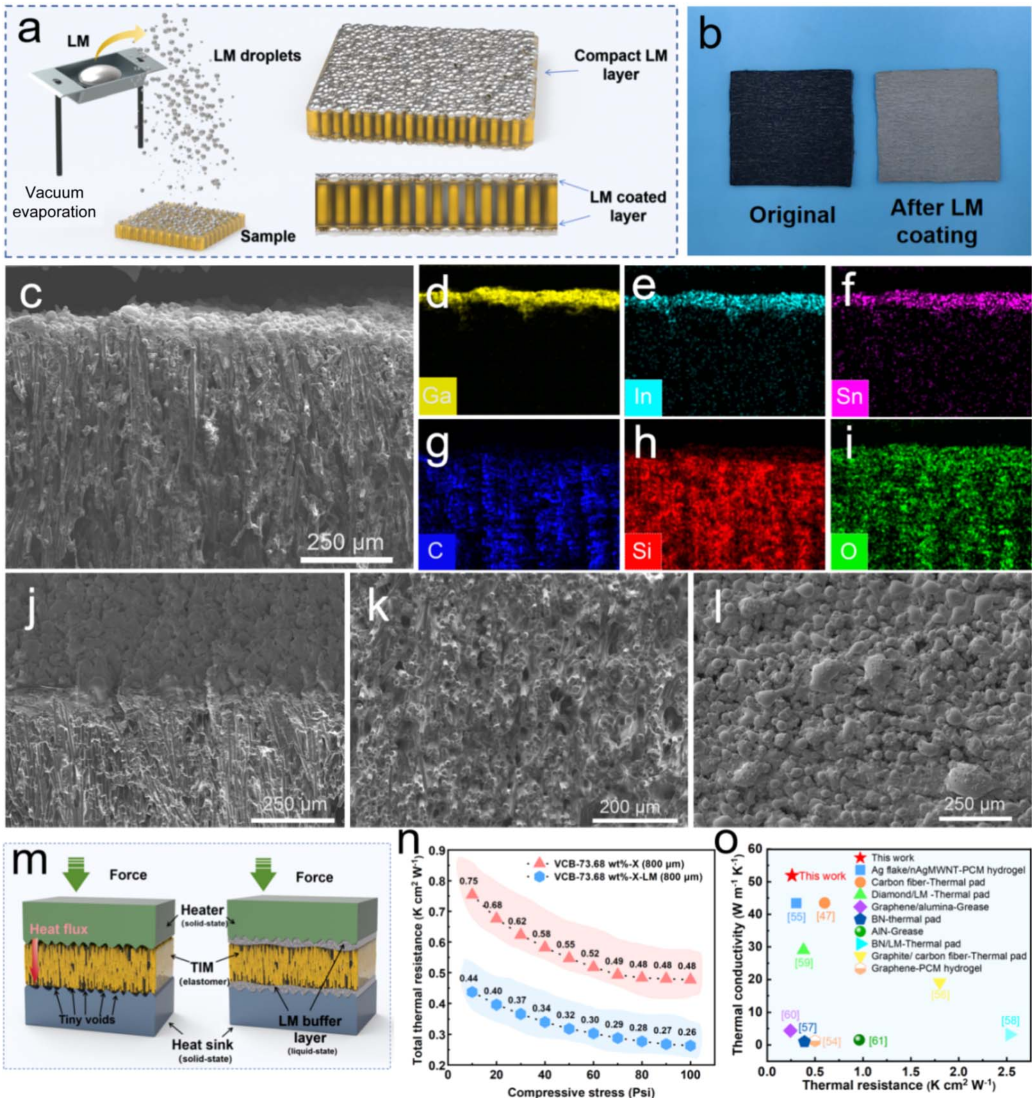

Fig. 5 Preparation and characterization of the functionalized coating. (a) Schematic diagram of the vacuum evaporation technique for coating LM onto composites. (b) Optical photography for the original composite and composite with LM coating. (c) The cross-section view of VCB-73.68 wt%-*X*-LM with the corresponding element mapping shown in (d)–(i). (j) Cross-section view of the microstructure of VCB-73.68 wt%-*X*-LM. (k) Top view of the microstructure of the composite without a coating. (l) Top view of the microstructure of the composite with an LM coating. (m) Schematic diagram of the contact state in the original composite and the LM coated composite. (n) Effect of compressive stress on the total thermal resistance of VCB-73.68 wt%-*X* and VCB-73.68 wt%-*X*-LM. (o) Comparison of total thermal resistance and thermal conductivity between VCB-73.68 wt%-*X*-LM and TIMs reported in the literature.

slope in the steady-state temperature *versus* input power plot, indicate values of 0.71 (commercial TIM), 0.81 (VCB-73.68 wt%-*X*), and 1.88 W cm^{-2} °C^{-1} (VCB-73.68 wt%-*X*-LM), respectively, showing the highest heat dissipation capability of VCB-73.68 wt%-*X*-LM. Furthermore, the thermal shock test was conducted on VCB-73.68 wt%-*X*-LM using the same setup, where the heater's power density was set to 0 and 80 W cm^{-2}. Fig. 6d illustrates the temperature variations of the heating plate over 2000 cycles, demonstrating that VCB-73.68 wt%-*X*-LM exhibits remarkable thermal stability.

Considering the exceptional heat transfer capabilities of the produced VCB-73.68 wt%-*X*-LM, we directly integrated it into a commercial desktop computer to validate its thermal behavior in real dynamic applications. As illustrated in Fig. 6e and depicted in the optical photograph, VCB-73.68 wt%-*X*-LM was packaged as a TIM between the Central Processing Unit (CPU, Inter core i5) and the air-cooled heat sink. Then, professional system diagnostic software (OCCT) was employed to drive the CPU to run at 100% usage. Meanwhile, the software HWINFO64 was utilized to monitor the temperature evolution of the CPU core and the effective clock frequency. For comparison, we conducted CPU stress tests under the same conditions using VCB-73.68 wt%-*X* and without using TIMs. As shown in Fig. 6f, under normal state, employing VCB-73.68 wt%-*X*-LM as the TIM decreased the temperature of the CPU core ($T_{\mathrm{CPU\ core}}$) by 4 °C compared to that without using the TIM, and it decreased by 2 °C

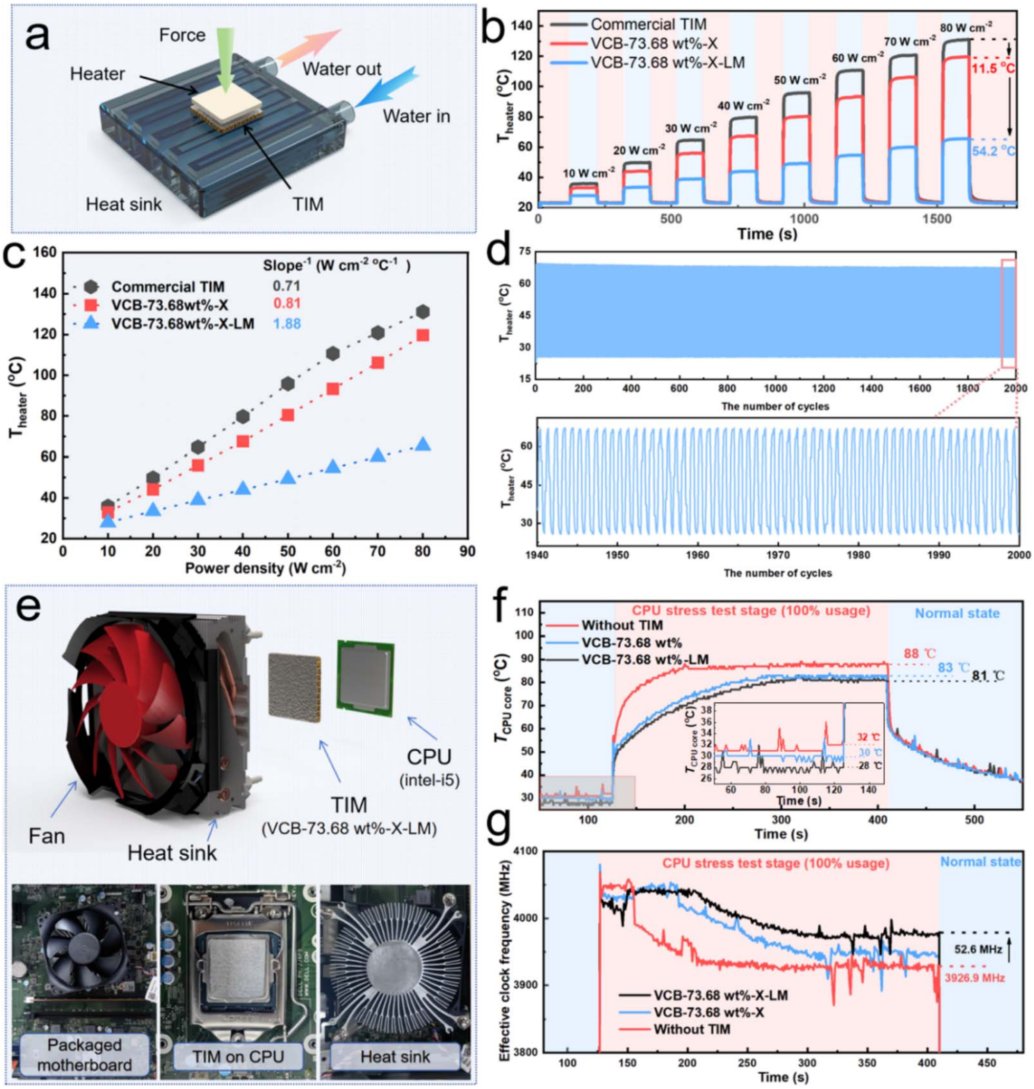

Fig. 6 TIM performance and the thermal management demonstration of VCB composites. (a) Schematic diagram of the TIM performance test system. (b) The evolution of heater temperature as a function of different power densities (10–80 W cm^{-2}) is compared between VCB composites and commercial TIM (Waretimo-WT5935C-250-65). (c) The correlation between the steady state temperature and power density of the heater. (d) Thermal shock stability tests in cyclic heating/cooling (2000 cycles) using VCB-73.68 wt%-*X*-LM as a TIM. (e) Assembly schematic diagram of the computer cooling system (inset photo showcasing the packaged motherboard and VCB-73.68 wt%-*X*-LM as a TIM applied on the CPU to bond the heat sink). (f) The evolution of CPU temperature during the CPU stress tests (100% CPU usage). (g) CPU effective clock variation during the CPU stress tests.

compared to using VCB-73.68 wt%-*X* as the TIM. During the stress test stage, the temperature gap increased notably. The $T_{\text{CPU core}}$ with VCB-73.68 wt%-*X*-LM as the TIM dropped by 8 °C compared to when no TIM was used. It also showed a 2 °C decrease compared to using VCB-73.68 wt%-*X* as the TIM. Here we noticed a discrepancy between the CPU test results and the TIM performance test results. It's important to note that during the CPU stress test, we utilized the existing commercial heat sink and fan, which have limited convective heat dissipation capabilities. While VCB-73.68 wt%-*X*-LM efficiently conducts CPU heat to the heat sink, the fan isn't able to promptly remove the heat from the heat sink, hindering the CPU temperature decrease. Despite the impact of the heat sink and fan on the TIM performance, as depicted in Fig. 6g, employing VCB-73.68 wt%-*X*-LM as the TIM resulted in an increased effective CPU clock frequency of 52.6 MHz compared to operating without a TIM. The increase in the effective CPU clock frequency directly enhances user experience, validating the potential application of VCB-73.68 wt%-*X*-LM as the TIM in the realm of consumer electronics.

Conclusions

In summary, we have developed a novel sandwich-structured CF thermal interface material, exhibiting exceptionally high through-plane thermal conductivity and lower thermal resistance. The central layer incorporates vertically aligned CFs to enhance $\kappa_{\perp}$, while the upper and lower layers were modified with liquid metal coatings to minimize the R_{contact}. The aligned

CF structures were obtained *via* a rolling-press technique, followed by stacking and cold-pressing processes to fabricate anisotropic block-shaped composites. Subsequent slicing of the composite yielded TIMs with vertically aligned heat conduction pathways. By utilizing quantitative analysis techniques such as micro-CT, we have successfully evaluated the perpendicularity of CFs and determined their effective fraction to be 59.14%. The VCB composite material demonstrates exceptional $\kappa_{\perp}$, achieving a remarkable value of 51.90 W m^{-1} K^{-1} at a filler loading of 73.68 wt%, surpassing the PDMS matrix by 323 times, while also exhibiting outstanding thermal stability and compressibility. Furthermore, it was observed that the $\kappa_{\perp}$ of the VCB composite material decreases with increasing deformation of compressed TIMs. Additionally, the liquid metal-modified layer transforms the contact state at the interface from "elastomer–solid" to "liquid–solid", resulting in a reduction in R_{total} of TIMs from 0.55 to 0.32 K cm^2 W^{-1} under an applied pressure of 50 psi. In practical CPU cooling verification, the VCB composite demonstrates exceptional heat transfer capability, offering potential applications in the consumer electronics field. This study not only provides insights into the structural design of CF-based TIMs but also proposes optimization solutions to address the high R_{contact} associated with the vertical CF structure, thereby enhancing their potential applications in the field of electronic thermal management.

Data availability

The data underlying this article will be shared on reasonable request to the corresponding author.

Author contributions

Zhenbang Zhang: conceptualization, methodology, writing – original draft; Rongjie Yang: software, data curation, writing – review & editing; Yandong Wang: methodology, formal analysis; Kang Xu: software, investigation, data curation; Wen Dai: formal analysis; Jianxiang Zhang: writing – review & editing; Maohua Li: investigation; Linhong Li: validation; Yingying Guo: validation; Yue Qin: visualization; Boda Zhu: visualization; Yiwei Zhou: writing – review & editing; Xingye Wang: data curation; Tao Cai: project administration; Cheng-Te Lin: project administration; Kazuhito Nishimura: resources; Hao Nan Li: supervision, writing – review & editing; Nan Jiang: supervision, writing – review & editing; Jinhong Yu: supervision, writing – review & editing.

Conflicts of interest

The authors declare no competing financial interest.

Acknowledgements

This research was funded by the Science and Technology Base and Talent Project of Guangxi (2022AC16005), the National Natural Science Foundation of China (52075527, 52102055), the National Key R&D Program of China (2022YFB3706602, 2021YFB3701801), Ningbo Key Scientific and Technological Project (2022Z191), the Yongjiang Talent Introduction Program of Ningbo (2021A-037-C, 2021A-108-G), Science and Technology Major Project of Ningbo (2021ZDYF020196, 2021ZDYF020198) and the Project of Chinese Academy of Science (ZDKYYQ2020001) and Ningbo 3315 Innovation Team (2019A-18-C).

References

1 X. Wang, C. Liu, Y. Wei, S. Feng, D. Sun and H. Cheng, *Mater. Today*, 2023, **63**, 170–187.
2 M. Samizadeh Nikoo and E. Matioli, *Nature*, 2023, **614**, 451–455.
3 J. S. Kang, M. Li, H. Wu, H. Nguyen, T. Aoki and Y. Hu, *Nat. Electron.*, 2021, **4**, 416–423.
4 B. Sun and X. Huang, *npj Flexible Electron.*, 2021, **5**, 12.
5 K. M. Razeeb, E. Dalton, G. L. W. Cross and A. J. Robinson, *Int. Mater. Rev.*, 2017, **63**, 1–21.
6 D. D. L. Chung, *Small*, 2022, **18**, e2200693.
7 J. Gu and K. Ruan, *Nano-Micro Lett.*, 2021, **13**, 110.
8 Z. Wang, Z. Wu, L. Weng, S. Ge, D. Jiang, M. Huang, D. M. Mulvihill, Q. Chen, Z. Guo, A. Jazzar, X. He, X. Zhang and B. B. Xu, *Adv. Funct. Mater.*, 2023, **33**, 2301549.
9 B. Xie, W. Zhao, X. Luo and R. Hu, *Mater. Sci. Eng.: R: Rep.*, 2023, **154**, 100738.
10 X. Xu, J. Chen, J. Zhou and B. Li, *Adv. Mater.*, 2018, **30**, e1705544.
11 Z. Xie, Z. Dou, D. Wu, X. Zeng, Y. Feng, Y. Tian, Q. Fu and K. Wu, *Adv. Funct. Mater.*, 2023, **33**, 2214071.
12 D. Pan, G. Yang, H. M. Abo-Dief, J. Dong, F. Su, C. Liu, Y. Li, B. Bin Xu, V. Murugadoss, N. Naik, S. M. El-Bahy, Z. M. El-Bahy, M. Huang and Z. Guo, *Nano-Micro Lett.*, 2022, **14**, 118.
13 K. Kim and J. Kim, *Composites, Part B*, 2016, **93**, 67–74.
14 N. Ye, J. Li, G. Zhang, Y. Lu, Z. Wang, H. Zhang and Y. Lu, *Chem. Mater.*, 2023, **35**, 5193–5203.
15 L. Jing, R. Cheng, M. Tasoglu, Z. Wang, Q. Wang, H. Zhai, S. Shen, T. Cohen-Karni, R. Garg and I. Lee, *Small*, 2023, **19**, e2207015.
16 T. Kim, S. Kim, E. Kim, T. Kim, J. Cho, C. Song and S. Baik, *Small*, 2021, **17**, e2102128.
17 B. Wei, X. Chen and S. Yang, *J. Mater. Chem. A*, 2021, **9**, 10979–10991.
18 C. Wang, Y. Gong, B. V. Cunning, S. Lee, Q. Le, S. R. Joshi, O. Buyukcakir, H. Zhang, W. K. Seong, M. Huang, M. Wang, J. Lee, G.-H. Kim and R. S. Ruoff, *Sci. Adv.*, 2021, **7**, eabe3767.
19 A. Minakov, J. Morikawa, M. Ryu, E. Zhuravlev and C. Schick, *Mater. Des.*, 2021, **201**, 109475.
20 Y. Zhang, G. Bai, X. Liu, J. Dai, X. Wang and H. Zhang, *J. Mater. Sci. Technol.*, 2021, **91**, 1–4.
21 M. Cao, Z. Li, J. Lu, B. Wang, H. Lai, Z. Li, Y. Gao, X. Ming, S. Luo, L. Peng, Z. Xu, S. Liu, Y. Liu and C. Gao, *Adv. Mater.*, 2023, **35**, e2300077.
22 G. Xiao, H. Li, Z. Yu, H. Niu and Y. Yao, *Nano-Micro Lett.*, 2023, **16**, 17.

23 Z. Zhang, M. Li, Y. Wang, W. Dai, L. Li, Y. Chen, X. Kong, K. Xu, R. Yang, P. Gong, J. Zhang, T. Cai, C.-T. Lin, K. Nishimura, H. N. Li, N. Jiang and J. Yu, *J. Mater. Chem. A*, 2023, **11**, 10971–10983.
24 H. Yu, Y. Feng, C. Chen, Z. Zhang, Y. Cai, M. Qin and W. Feng, *Carbon*, 2021, **179**, 348–357.
25 W. Feng, M. Qin and Y. Feng, *Carbon*, 2016, **109**, 575–597.
26 X. Hou, Y. Chen, W. Dai, Z. Wang, H. Li, C.-T. Lin, K. Nishimura, N. Jiang and J. Yu, *Chem. Eng. J.*, 2019, **375**, 121921.
27 K. Uetani, S. Ata, S. Tomonoh, T. Yamada, M. Yumura and K. Hata, *Adv. Mater.*, 2014, **26**, 5857–5862.
28 Q. Wu, W. Li, C. Liu, Y. Xu, G. Li, H. Zhang, J. Huang and J. Miao, *Carbon*, 2022, **187**, 432–438.
29 M. Li, Z. Ali, X. Wei, L. Li, G. Song, X. Hou, H. Do, J. C. Greer, Z. Pan, C.-T. Lin, N. Jiang and J. Yu, *Composites, Part B*, 2021, **208**, 108599.
30 G. Zhang, S. Xue, F. Chen and Q. Fu, *Compos. Sci. Technol.*, 2023, **231**, 109784.
31 J. Ma, T. Shang, L. Ren, Y. Yao, T. Zhang, J. Xie, B. Zhang, X. Zeng, R. Sun, J.-B. Xu and C.-P. Wong, *Chem. Eng. J.*, 2020, **380**, 122550.
32 B. Wu, J. Li, X. Li, G. Qian, P. Chen, R. Xia and J. Qian, *Composites, Part A*, 2021, **150**, 106623.
33 R. Huang, D. Ding, X. Guo, C. Liu, X. Li, G. Jiang, Y. Zhang, Y. Chen, W. Cai and X.-a. Zhang, *Compos. Sci. Technol.*, 2022, **230**, 109717.
34 S. Han, Y. Ji, Q. Zhang, H. Wu, S. Guo, J. Qiu and F. Zhang, *Nano-Micro Lett.*, 2023, **15**, 146.
35 H. Chen, W. Zhu, H. Tang and W. Yan, *Int. J. Mach. Tool Manufact.*, 2021, **163**, 103703.
36 R. Mason and J. T. Koberstein, *J. Adhes.*, 2005, **81**, 765–789.
37 I. Mochida, S. H. Yoon, N. Takano, F. Fortin, Y. Korai and K. Yokogawa, *Carbon*, 1996, **34**, 941–956.
38 Y. Sugimoto, D. Shimamoto, Y. Hotta and H. Niino, *Carbon Trends*, 2022, **9**, 100194.
39 A. Yamanaka, M. Terada, M. Ichiki, Y. Kimoto, K. Shiraki, M. Nagata, D. Shimamoto and Y. Hotta, *J. Fiber Sci. Technol.*, 2020, **76**, 199–207.
40 L. Guo, Z. Zhang, M. Li, R. Kang, Y. Chen, G. Song, S.-T. Han, C.-T. Lin, N. Jiang and J. Yu, *Compos. Commun.*, 2020, **19**, 134–141.
41 T. Ji, Y. Feng, M. Qin, S. Li, F. Zhang, F. Lv and W. Feng, *Carbon*, 2018, **131**, 149–159.
42 Z. Yu, S. Wei and J. Guo, *J. Mater. Sci.: Mater. Electron.*, 2019, **30**, 10233–10243.
43 D. Ding, R. Huang, X. Wang, S. Zhang, Y. Wu, X.-a. Zhang, G. Qin, Z. Liu, Q. Zhang and Y. Chen, *Chem. Eng. J.*, 2022, **441**, 136104.
44 F. Huang, W. Qin, D. Shu, J. Sun, J. Li, D. Meng, W. Yue and C. Wang, *Ceram. Int.*, 2023, **49**, 32971–32978.
45 P. Zhang, Y. Qiu, C. Ye and Q. Li, *Chem. Eng. J.*, 2023, **461**, 141940.
46 Z. Zhang, J. Wang, J. Shang, Y. Xu, Y. J. Wan, Z. Lin, R. Sun and Y. Hu, *Small*, 2023, **19**, e2205716.
47 J. Li, Z. Ye, P. Mo, Y. Pang, E. Gao, C. Zhang, G. Du, R. Sun and X. Zeng, *Compos. Sci. Technol.*, 2023, **234**, 109948.
48 T. Jiao, B. Han, L. Zhao, Z. Zhang, Y. Zeng, D. Li, K. Zhang, Q. Deng, Y. Zhao and Z. Li, *Appl. Surf. Sci.*, 2023, **618**, 156711.
49 L. Xu, K. Zhan, S. Ding, J. Zhu, M. Liu, W. Fan, P. Duan, K. Luo, B. Ding, B. Liu, Y. Liu, H. M. Cheng and L. Qiu, *ACS Nano*, 2023, **17**, 4886–4895.
50 N. Zhao, J. Li, W. Wang, W. Gao and H. Bai, *ACS Nano*, 2022, **16**, 18959–18967.
51 H. He, W. Peng, J. Liu, X. Y. Chan, S. Liu, L. Lu and H. Le Ferrand, *Adv. Mater.*, 2022, **34**, e2205120.
52 C. Lei, Y. Zhang, D. Liu, X. Xu, K. Wu and Q. Fu, *Compos. Sci. Technol.*, 2021, **214**, 108995.
53 W. Jang, S. Lee, N. R. Kim, H. Koo, J. Yu and C.-M. Yang, *Composites, Part B*, 2023, **248**, 110355.
54 J. Yang, W. Yu, C. Liu, H. Xie and H. Xu, *Compos. Sci. Technol.*, 2022, **219**, 109223.
55 S. A. Abdul Jaleel, T. Kim and S. Baik, *Adv. Mater.*, 2023, **35**, e2300956.
56 M. Li, L. Li, X. Hou, Y. Qin, G. Song, X. Wei, X. Kong, Z. Zhang, H. Do, J. C. Greer, F. Han, T. Cai, W. Dai, C.-T. Lin, N. Jiang and J. Yu, *Compos. Sci. Technol.*, 2021, **212**, 108883.
57 Y. Ji, S.-D. Han, H. Wu, S.-Y. Guo, F.-S. Zhang and J.-H. Qiu, *Chin. J. Polym. Sci.*, 2024, **42**, 352–363.
58 Z. Wang, J. Li, N. Ye, H. Zhang, D. Yang and Y. Lu, *Compos. Sci. Technol.*, 2023, **233**, 109903.
59 S. Wei, W. Wang, L. Zhou and J. Guo, *Composites, Part A*, 2022, **162**, 107149.
60 C. Chen, Y. He, C. Liu, H. Xie and W. Yu, *J. Mater. Sci.: Mater. Electron.*, 2020, **31**, 4642–4649.
61 P. Luo, Y. Tuersun, X. Huang, H. Yang and S. Chu, *Adv. Eng. Mater.*, 2023, **25**, 2301092.